Towards time-resolved serial crystallography in a microfluidic device

Ashtamurthy S. Pawate,[a] Vukica Šrajer,[b] Jeremy Schieferstein,[a] Sudipto Guha,[a] Robert Henning,[b] Irina Kosheleva,[b] Marius Schmidt,[c] Zhong Ren,[b,d] Paul J. A. Kenis[a] and Sarah L. Perry[a,e]*

[a]Department of Chemical and Biomolecular Engineering, The University of Illinois at Urbana-Champaign, Urbana, Illinois, USA, [b]Center for Advanced Radiation Sources, The University of Chicago, Argonne, Illinois, USA, [c]Department of Physics, The University of Wisconsin Milwaukee, Milwaukee, Wisconsin, USA, [d]Renz Research Inc., Westmont, Illinois, USA, and [e]Department of Chemical Engineering, The University of Massachusetts Amherst, Amherst, Massachusetts, USA. *Correspondence e-mail: perrys@engin.umass.edu

Serial methods for crystallography have the potential to enable dynamic structural studies of protein targets that have been resistant to single-crystal strategies. The use of serial data-collection strategies can circumvent challenges associated with radiation damage and repeated reaction initiation. This work utilizes a microfluidic crystallization platform for the serial time-resolved Laue diffraction analysis of macroscopic crystals of photoactive yellow protein (PYP). Reaction initiation was achieved via pulsed laser illumination, and the resultant electron-density difference maps clearly depict the expected pR_1/pR_{E46Q} and pR_2/pR_{CW} states at 10 µs and the pB_1 intermediate at 1 ms. The strategies presented here have tremendous potential for extension to chemical triggering methods for reaction initiation and for extension to dynamic, multivariable analyses.

1. Introduction

Developments in the field of protein crystallography continue to enable structural analysis of ever-smaller crystals and more challenging targets. However, the ultimate goal remains the direct observation of functional motions within a protein. The challenge of obtaining dynamic structural information stems from (i) the necessary X-ray exposure times for obtaining a diffraction pattern, which are typically on the order of milliseconds to seconds for monochromatic, synchrotron radiation, compared with femtoseconds to milliseconds for functional motions in proteins, (ii) the large X-ray dose required for the collection of data at multiple time points during a reaction and (iii) difficulties associated with synchronizing macromolecular dynamics within protein crystals.

Traditionally, time-resolved crystallography has been enabled through the use of polychromatic, Laue diffraction (Ren *et al.*, 1999). At synchrotron sources, Laue diffraction enables data collection with a time resolution of ∼100 ps, the duration of a synchrotron X-ray pulse (Moffat, 1997, 2014; Graber *et al.*, 2011). Polychromatic radiation allows a significant fraction of the reflections (reciprocal space) to be in a diffracting condition during exposure, resulting in significantly shorter exposure times compared with monochromatic diffraction and allowing the measurement of integrated diffraction peaks without sample oscillation (Hedman *et al.*, 1985; Cornaby *et al.*, 2010). More recently, ultrabrilliant X-ray free-electron lasers (XFELs) have enabled data collection

Arg52

p-Coumaric Acid

Cys69

Accumulated pB1
Microfluidic
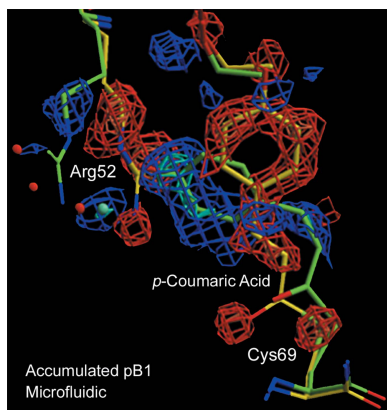
using single femtosecond X-ray pulses (Neutze & Moffat, 2012; Kupitz *et al.*, 2014; Tenboer *et al.*, 2014).

However, for both the Laue method and XFELs, the high X-ray flux results in significant radiation damage, a challenge that is exacerbated by the need to perform data collection at biologically relevant temperatures and map out structural changes in the time domain. The effects of radiation damage can be circumvented by taking advantage of an approach termed 'serial crystallography' (Chapman *et al.*, 2011; Hunter & Fromme, 2011), which extends the concept of combining data from multiple crystals (Yonath *et al.*, 1998; Cherezov *et al.*, 2007; Cornaby *et al.*, 2010; Liu, Chen *et al.*, 2011; Liu, Zhang *et al.*, 2011; Liu *et al.*, 2012; Liu, Liu *et al.*, 2013) to the limit of a single frame of data per crystal. This approach has been critical for structural biology efforts at XFEL sources, where radiation damage only allows the collection of a single diffraction image from each crystal (Hedman *et al.*, 1985; Chapman *et al.*, 2011; Boutet *et al.*, 2012; Johansson *et al.*, 2012, 2013; Smith *et al.*, 2012; Barends *et al.*, 2013; Demirci *et al.*, 2013; Kern *et al.*, 2013, 2014; Redecke *et al.*, 2013; Hirata *et al.*, 2014; Kupitz *et al.*, 2014; Tenboer *et al.*, 2014). Serial methods have been extended to analysis at synchrotron sources (Wang *et al.*, 2012; Gati *et al.*, 2014; Heymann *et al.*, 2014; Stellato *et al.*, 2014), including for Laue methods (Dejoie *et al.*, 2013; Perry *et al.*, 2014). However, these large-scale serial crystallography methods suffer from the need to manipulate crystals and/or from inefficient sample utilization (Chapman *et al.*, 2011; Zarrine-Afsar *et al.*, 2012; Liu, Wacker *et al.*, 2013; Hunter *et al.*, 2014; Lyubimov *et al.*, 2015).

For time-resolved studies, detection of transient structural intermediates requires a rapid triggering event, or pump (for example, light or a temperature jump), to synchronize structural changes within a crystal that are then probed by short X-ray pulses. Traditionally, one crystal or a small number of crystals are used for data collection, which requires multiple pump–probe cycles on the same crystal volume for the collection of complete data at different time points and crystal orientations. This is feasible if the reaction is reversible and the protein undergoes a complete reaction cycle and naturally resets to the initial state before the next pump–probe cycle (Neutze & Moffat, 2012; Ren *et al.*, 2012; Schotte *et al.*, 2012; Jung *et al.*, 2013; Schmidt *et al.*, 2013; Kupitz *et al.*, 2014; Moffat, 2014). Unfortunately, many reactions in crystals are either irreversible or are effectively irreversible owing to radiation damage, slow timescales for reversion to the initial state or limitations of the crystal lattice (Moffat, 1997, 2014; Graber *et al.*, 2011; Miller, 2014). To facilitate studies of irreversible processes, a large number of crystals or crystal volumes is necessary since only one trigger event is possible for each fresh crystal (volume). This also requires methods for rapid sample exchange, and standard methods for room-temperature crystal mounting are not appropriate for such data collection. As a result, even when a means for rapid triggering is available, many important biological systems have been resistant to classical time-resolved crystallography. However, serial time-resolved approaches have recently been demonstrated using laser photoinitiation and XFEL sources to analyze photosystem II and photoactive yellow protein (PYP) (Ren *et al.*, 1999; Kupitz *et al.*, 2014; Tenboer *et al.*, 2014). Instead of repeated photoinitiation on the same crystal, these experiments took advantage of a liquid jet for rapid crystal delivery into the X-ray beam and averaging of data from a very large number of crystals.

Recently, we reported a low-profile microfluidic platform for protein crystallization that eliminates manual handling of protein crystals and was used effectively for the serial collection of Laue diffraction data at a synchrotron source (Perry *et al.*, 2014) and for anomalous diffraction analysis (Perry *et al.*, 2013). Our approach enables the reproducible growth of isomorphous crystals with low mosaicity (Guha *et al.*, 2012; Perry *et al.*, 2013) and provides an alternative platform for the implementation of large-scale serial crystallography with higher sample utilization than liquid (Chapman *et al.*, 2011) or paste jets (Liu, Wacker *et al.*, 2013) and without the need for sample manipulation associated with fixed target-based strategies (Zarrine-Afsar *et al.*, 2012; Hunter *et al.*, 2014; Lyubimov *et al.*, 2015) reported previously. Furthermore, our platform is compatible with optical methods for reaction initiation, and integrated fluidic control could be used to enable chemical triggering and/or the formulation of a wide range of sample conditions for dynamic crystallography experiments (Ren *et al.*, 2013).

Here, we present, for the first time, the application of our microfluidic crystallization platform for time-resolved data collection using synchrotron Laue radiation. We validate our approach by merging data collected from multiple crystals of PYP grown on-chip, first using repeated photoinitiation to drive the accumulation of the pB_1 intermediate in a steady-
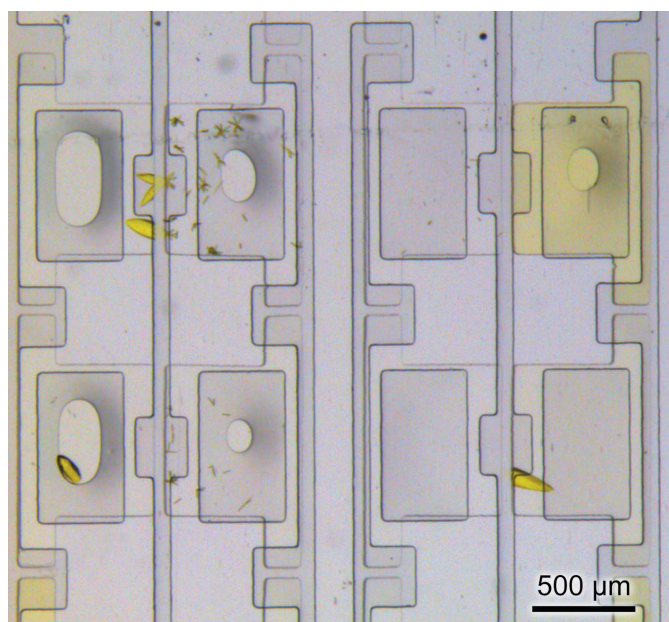

Figure 1
Optical micrograph of PYP crystals grown in a microfluidic crystallization platform showing a view of four wells from a larger 96-well chip. Micro-seed solution was filled into the middle sets of half-wells and a mixture of protein and precipitant was introduced into the outside sets of half-wells. Crystals formed after mixing and overnight incubation.

500 μm

state-like experiment, followed by the collection of time-resolved data to probe transient structural changes on the microsecond and millisecond timescales.

2. Methods

2.1. Expression and purification of PYP

Polyhistidine-tagged apo PYP from *Halorhodospira halophila* BN9626 was heterologously expressed and purified from *Escherichia coli*, reconstituted to holo PYP with the chromophore *p*-coumaric acid and treated with enterokinase to cleave the polyhistidine tag using procedures reported previously (Kort *et al.*, 1996).

2.2. Fabrication and operation of microfluidic crystallization devices

Crystallization chips were fabricated and operated as described previously (Guha *et al.*, 2012; Khvostichenko *et al.*, 2013; Perry *et al.*, 2013, 2014). The microfluidic chip design consists of separate half-wells for protein/precipitant and micro-seed solutions (Fig. 1). Dedicated valve lines for each set of half-wells allow independent filling with the protein/precipitant solution and the seeding solution.

2.3. Crystallization of PYP

PYP was crystallized in microfluidic chips using previously published crystallization conditions (Yamaguchi *et al.*, 2007). The PYP crystals were crushed in 3 *M* ammonium sulfate to prepare a microseed stock solution from which serial dilution was carried out by successively diluting 50% of the microseed solution into 3 *M* ammonium sulfate. PYP was then crystallized in 96-well microfluidic chips by microseeding. A 1:1 mixture of 20 mg ml^{-1} PYP (in 10 m*M* HEPES pH 7.4, 50 m*M*

NaCl) and 2.6 *M* ammonium sulfate was loaded into one set of half-wells, while a PYP micro-seed solution in 3 *M* ammonium sulfate was loaded into the corresponding adjacent chamber. A microseed serial dilution of 1:12.5 from the original stock solution produced 1–2 crystals per chamber and was used in all subsequent crystallization experiments. One complete chip required 6 µl protein/precipitant solution and 6 µl microseed solution. Ammonium sulfate at pH 5.0 was used for the initial set of experiments. The pH was adjusted to 7.0 for time-resolved experiments. The isolation valve between the two half-wells was actuated for 20 min to allow mixing of the two solutions by free-interface diffusion. Crystals grew to variable dimensions after incubation overnight at room temperature (Fig. 1).

2.4. On-chip X-ray diffraction

Data were collected in polychromatic mode at 12 keV (1.03 Å, 5% bandwidth) on the 14-ID-B beamline (Graber *et al.*, 2011) at the Advanced Photon Source at Argonne National Laboratory. The microfluidic chips were mounted directly on the φ spindle of the goniometer (Fig. 2). Positioning and alignment of the chips was performed using a high-resolution camera oriented at 30° with respect to the X-ray beam and a medium-resolution camera oriented at 60°, as described previously (Perry *et al.*, 2014). Sample visualization and positioning were performed using a graphical user interface with the in-house *uControl* software at the 14-ID-B beamline. Sample positioning was achieved using a click-and-translate routine coupled to the high- and medium-resolution cameras. Sample centering along the path of the X-ray beam was achieved by visually focusing the sample, taking advantage of the very small depth of field of the high-resolution
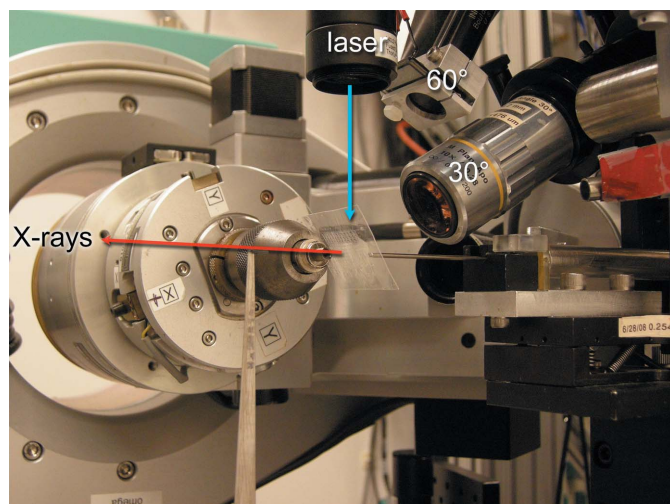

Figure 2
A 96-well chip mounted on the 14-ID-B beamline at BioCARS. The triggering laser and high-resolution (30°) and medium-resolution (60°) cameras are indicated. The chip is facing the high-resolution camera. The red arrow indicates the incident X-ray beam; the cyan arrow indicates the incident laser beam.
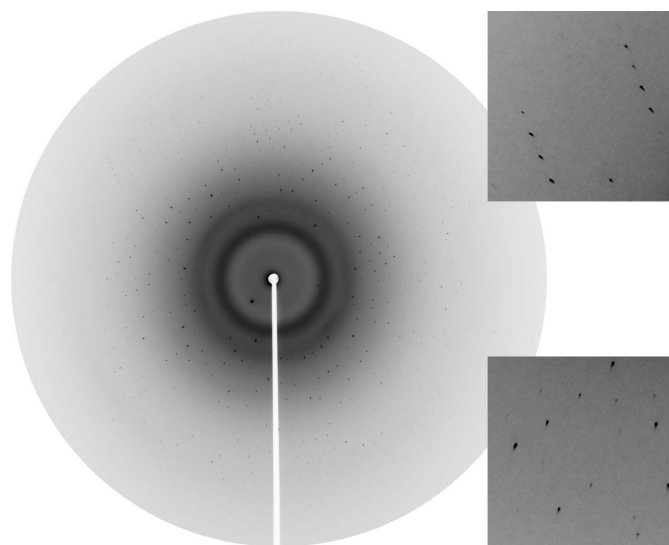

Figure 3
In situ Laue diffraction from a PYP crystal on-chip. Diffraction spots can clearly be observed, even when coincident with the diffuse background scattering from the polymer materials of the chip. The inset images provide more detail of the quality and intensity at high Bragg angles. The sample-to-detector distance was 110 mm.

Table 1
Crystallographic statistics for data with an accumulated pB_1 state obtained using on-chip serial Laue analysis.

Values in parentheses are for the highest resolution shell.

Data set	Dark	Accumulated pB_1
No. of crystals	5	5
No. of images	30	29
Resolution (Å)	100–1.80 (1.88–1.80)	100–1.80 (1.88–1.80)
Space group	$P6_3$	$P6_3$
Unit-cell parameters (Å)	$a = 66.9$, $b = 66.9$, $c = 41.0$	$a = 66.9$, $b = 66.9$, $c = 41.0$
Single reflections		
$R_{merge}(F^2)$	0.075	0.087
$R_{merge}(F)$	0.047	0.054
$\langle F/\sigma(F) \rangle$	37.0 (26.8)	32.6 (20.2)
Total observations	27306 (1766)	23432 (1333)
Unique observations	8414 (778)	8061 (710)
Multiplicity	3.2 (2.2)	2.9 (1.9)
Single and harmonic reflections		
Unique observations	8500 (785)	8121 (713)
Completeness (%)	87.1 (67.0)	83.2 (60.7)

Table 2
Crystallographic statistics for time-resolved data obtained using on-chip serial Laue analysis.

Values in parentheses are for the highest resolution shell.

Data set	Dark	10 µs	10 ms
No. of crystals	10	10	10
No. of images	22	21	22
Resolution (Å)	100–1.80 (1.88–1.80)	100–1.80 (1.88–1.80)	100–1.80 (1.88–1.80)
Space group	$P6_3$	$P6_3$	$P6_3$
Unit-cell parameters (Å)	$a = 66.9$, $b = 66.9$, $c = 41.0$	$a = 66.9$, $b = 66.9$, $c = 41.0$	$a = 66.9$, $b = 66.9$, $c = 41.0$
Single reflections			
$R_{merge}(F^2)$	0.074	0.080	0.081
$R_{merge}(F)$	0.043	0.046	0.047
$\langle F/\sigma(F) \rangle$	37.5 (34.4)	35.2 (31.6)	34.4 (28.5)
Total observations	18517 (980)	17044 (842)	17389 (944)
Unique observations	7393 (573)	7134 (527)	7247 (522)
Multiplicity	2.5 (1.7)	2.4 (1.6)	2.4 (1.8)
Single and harmonic reflections			
Unique observations	7456 (578)	7189 (529)	7301 (559)
Completeness (%)	76.8 (49.8)	74.0 (45.4)	75.3 (48.2)

camera. The interface enabled identification and alignment of all crystals on a chip followed by automated data collection. *uControl* interacts with the BioCARS timing module and the *LaueCollect* software for control of the laser pulse for photocycle initiation followed by X-ray exposure after an appropriate time delay.

Initiation of the PYP photocycle was achieved using nanosecond pulses from a Nd:YAG/OPO laser (OPOTEK Opolette 355 II HE; 7 ns pulse duration; 20 Hz). The laser beam was focused to a spot size of 100×100 µm at the sample, delivering 4.8 mJ mm^{-2} at 485 nm. The laser beam path was perpendicular with respect to the X-ray beam (Fig. 2). Data were collected from microfluidic chips initially oriented at 30° with respect to the X-ray beam (*i.e.* parallel to the high-resolution camera). The robust PYP crystals permitted the potential collection of multiple frames of data from each individual crystal at room temperature (Fig. 3). For strongly diffracting crystals, light and dark data were collected at 5° intervals over the range 20–40° from stationary crystals. For complete data sets, data were merged from multiple crystals (see Tables 1 and 2). The X-ray beam was 90×70 µm. A MAR CCD 165 detector was used with a sample-to-detector distance of 110 mm.

Two strategies for data collection were pursued. Initial experiments were performed in a steady-state-like measurement (Genick *et al.*, 1997) where the crystal was exposed to a repeated pump–probe sequence (pump, 5 ns laser pulse; probe, an X-ray pulse train of 18 individual X-ray pulses generated by the storage ring operating in 324 singlet mode, delayed by 1 ms from the laser pulse, with a 2 s wait time between each photocycle initiation). Here, the accumulation of 80 pump–probe sequences was used for each diffraction frame prior to detector readout. The wait time used in this experiment was insufficient for the protein photocycle to reset to the dark state at pH 5.0 (Tripathi *et al.*, 2012), thus driving the accumulation of high concentrations of the pB_1 intermediate by the end of 80 pump–probe sequences.

A second set of experiments was designed to collect actual time-resolved structural information. For these experiments, crystals were grown at pH 7.0 in order to accelerate the recovery time of the photocycle (Tripathi *et al.*, 2012). Here, the accumulation of ten pump–probe sequences was used for each diffraction frame prior to detector readout: pump, 5 ns laser pulse; probe, an X-ray pulse train of 11 individual X-ray pulses generated by the storage ring operating in 24-bunch mode, delayed by either 10 µs or 1 ms from the laser pulse, with a 3 s wait time between photocycle initiations to enable full recovery to the ground state. From each crystal, a dark, laser-off diffraction frame was collected followed by a sequence of two laser-on diffraction frames at 10 µs and 1 ms after photocycle initiation.

2.5. Data analysis

Laue diffraction images were processed with the *Precognition/Epinorm* software (Renz Research; Tables 1 and 2). Each crystal was indexed separately and data from multiple crystals were merged. PYP crystallizes in space group $P6_3$, which allows two alternative indexing conventions, which were selected randomly by the software during indexing. Prior to merging the data from different crystals, this indexing ambiguity had to be resolved. For the steady-state-like accumulation of the pB_1 intermediate, this indexing ambiguity was handled manually. Data were merged for each new crystal with the previously processed crystals using both indexing alternatives: (*hkl*) *versus* (*khl*). The values of R_{merge} were then compared to determine the consistent indexing alternative. For the time-resolved data we took advantage of new software developed by M. Schmidt that makes use of the Pearson (cross) correlation coefficient (Brehm & Diederichs, 2014) between intensities of symmetry-related reflections found in two diffraction patterns taking a previously known lambda

curve into account. The resulting cross-correlation matrix is then diagonalized and the indexing convention is recovered
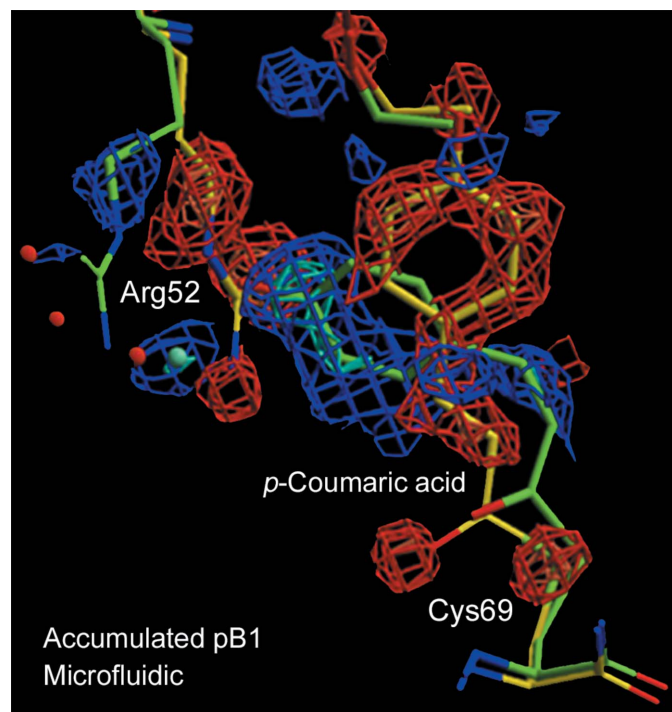

Figure 4
Difference electron-density map of PYP depicting the structural changes in the chromophore binding pocket, including conformational changes of the *p*-coumaric acid, Arg52 and Cys69 that occur owing to accumulation of the pB$_1$ intermediate, compared with the dark state. Maps are contoured at $\pm 3\sigma$ and $\pm 5\sigma$ and are superimposed on a stick representation of the protein structure in the dark state (yellow, PDB entry 2phy) and the pB1 intermediate (green, PDB entry 1ts0).

from the second eigenvector. Negative entries of this eigenvector mean flip the indices from *hkl* to *khl*, while positive entries mean keep the indexing convention. The data were integrated to 1.80 Å resolution (Tables 1 and 2). This resolution was chosen both to maintain a completeness in the highest resolution shell, on the order of 50%, and based on the quality of the subsequent electron-density difference maps.

Weighted difference electron-density maps for various time points (Figs. 4 and 5) were calculated using weighted difference structure-factor (SF) amplitudes $\Delta F_w = w[|F_{light}(t)| - |F_{dark}|]$ and phases derived from the reference PYP structure (PDB entry 2phy; Borgstahl *et al.*, 1995). $|F_{dark}|$ is the laser-off SF amplitude and $|F_{light}(t)|$ is the corresponding laser-on SF amplitude at time t (Ren *et al.*, 2001). The R_{cryst} between F_{dark} and F_{calc} (2phy) is 19.6% without further structural refinement. The weight w was calculated as (Ren *et al.*, 2001)

$$w = \frac{1}{\left(1 + \frac{\Delta F^2}{\langle|\Delta F|\rangle^2} + \frac{\sigma_{\Delta F}^2}{\langle\sigma_{\Delta F}\rangle^2}\right)}, \qquad (1)$$

where $\Delta F = |F_{light}(t)| - |F_{dark}|$ is the difference in the SF amplitudes between time t and the dark state. $\sigma_{\Delta F}^2 = \sigma^2(F_{dark}) + \sigma^2[F_{light}(t)]$ is the variance of ΔF determined as the sum of the variances of F_{dark} and $F_{light}(t)$. The symbol $\langle x \rangle$ denotes the mean value of x in a data set. Difference electron-density maps (Figs. 4 and 5) were calculated and displayed in *XtalView* (McRee, 1993). Maps were contoured at $\pm 3\sigma$ and $\pm 5\sigma$, where σ is the root-mean-square value of the difference electron density across the asymmetric unit. Time-resolved maps were compared with data collected from a single, large, capillary-mounted PYP crystal on 14-ID-B using the methods described in Schmidt *et al.* (2013). Models of the pR$_1$/pR$_{E46Q}$ and pR$_2$/
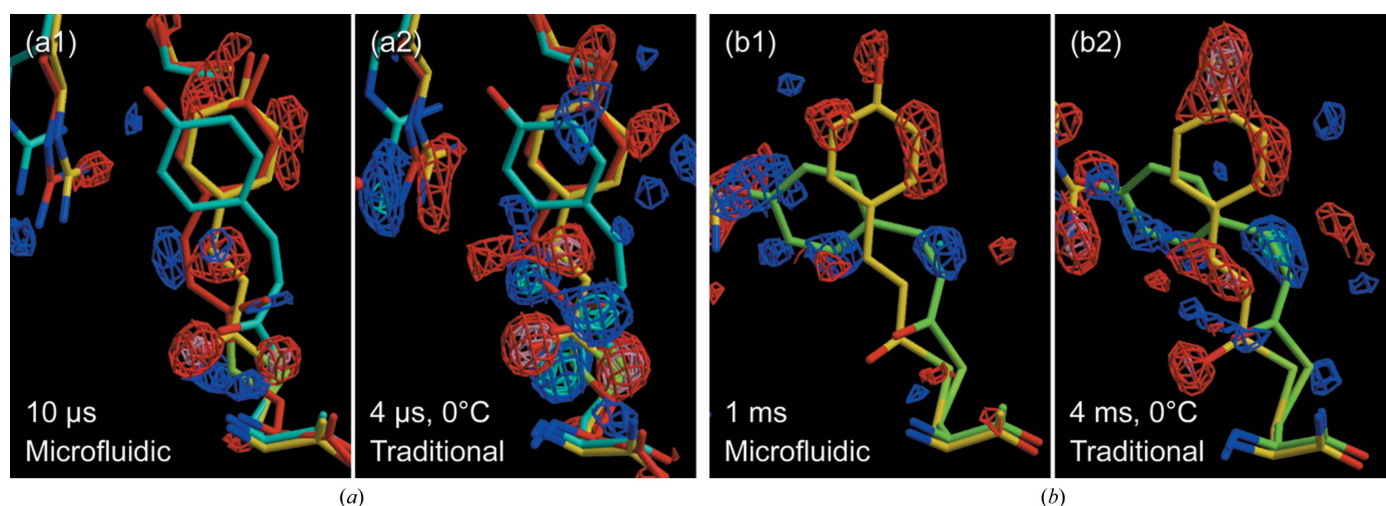

Figure 5
Difference electron-density maps of PYP depicting the structural changes in the chromophore binding pocket, including conformational changes of the *p*-coumaric acid that occur (*a*) 4–10 µs after photoinitiation and (*b*) 1–4 ms after photoinitiation. The left-hand maps (a1 and b1) show the data obtained using our microfluidic approach at room temperature. We compare this with those (right; a2 and b2) for data collected from a large single crystal mounted in a traditional glass capillary at 0°C (Schmidt *et al.*, 2013). Although the temperature was different for the maps shown, in both cases data were collected in the time domain where the concentrations of the intermediates plateaued (Schmidt *et al.*, 2013) and similar signal is expected for both maps. Maps are contoured at $\pm 3\sigma$ and $\pm 5\sigma$ and are superimposed on a stick representation of the protein structure in the dark state (yellow, PDB entry 2phy), the pR$_1$/pR$_{E46Q}$ state (cyan, PDB entry 1ts7), the pR$_2$/pR$_{CW}$ state (red, PDB entry 1ts7) and the pB1 intermediate (green, PDB entry 1ts0).

pR_{CW} intermediates were obtained from PDB entry 1ts7 and that of pB_1 from PDB entry 1ts0 (Ihee *et al.*, 2005).

3. Results and discussion

The goal of this work was to demonstrate the feasibility of time-resolved protein crystallography *via* serial Laue crystallography in a microfluidic device. The bacterial blue light photoreceptor photoactive yellow protein (PYP) was used as a model system since its photocycle has been very well characterized by a number of previous standard time-resolved crystallographic studies. The on-chip crystallization and the collection of serial Laue diffraction data have been reported previously (Perry *et al.*, 2014), as has the successful collection of single-wavelength anomalous diffraction for *de novo* structure determination (Perry *et al.*, 2013). These results suggested the strong potential for observing the type of small structural changes anticipated in a time-resolved diffraction experiment.

PYP crystals form in a needle-like crystal habit, with typical dimensions of $10–60 \times 10–60 \times 100–300$ µm as crystallized on-chip (Fig. 1). For this work, multiple orientations as well as both dark and light data were collected from a limited number of crystals and were used to demonstrate the proof-of-concept feasibility of our approach. This data-collection strategy was facilitated by the stability of PYP crystals, which successfully resist significant radiation damage (Schmidt *et al.*, 2012).

For initial experiments, a repeated pump–probe sequence was used to drive the accumulation of the pB_1 intermediate. Crystallization was performed at pH 5.0, where recovery to the ground state is slow (Tripathi *et al.*, 2012). 30 frames of laser-off and laser-on data were collected from five crystals to a resolution of 1.80 Å and merged into data sets that were 87.1 and 83.2% complete for the dark state and the accumulated pB_1 state, with $R_{merge}(F)$ values of 0.047 and 0.054, respectively (Table 1). The resulting electron-density difference map clearly depicts the formation of pB_1 (Fig. 4). The transition between the dark state and pB_1 is characterized by *trans*-to-*cis* isomerization of the *p*-coumaric acid chromophore as well as opening of the Arg52 gate. The areas of positive and negative electron density observed in Fig. 4 match well similar results reported previously (Genick *et al.*, 1997; Schmidt *et al.*, 2004; Ihee *et al.*, 2005).

Time-resolved experiments were designed to examine the regimes where pR states and the pB state are dominant. At 10 µs, the pR_1/pR_{E46Q} and pR_2/pR_{CW} states are expected, while at 1 ms pB_1 is anticipated (Fig. 5). Data from 22 frames and ten crystals were merged to a resolution of 1.80 Å with completenesses of 76.8, 74.0 and 75.3% and $R_{merge}(F)$ values of 0.043, 0.046 and 0.047 for the dark, 10 µs and 1 ms data, respectively (Table 2). Our crystals diffracted to a similar resolution as traditional, single-crystal reports for PYP: 1.80 Å compared with 1.60–1.80 Å (Tripathi *et al.*, 2012; Schmidt *et al.*, 2013). Our results also match well with reports from traditional single-crystal Laue reports in terms of $R_{merge}(F)$ and completeness (Tripathi *et al.*, 2012; Schmidt *et al.*, 2013).

We compared the electron-density difference maps obtained from on-chip data with maps obtained using traditional single-crystal methods (Fig. 5; Schmidt *et al.*, 2013). The data of Schmidt and coworkers were obtained at slightly different delay times compared with our data (4 µs instead of 10 µs and 4 ms instead of 1 ms) and at 0°C instead of room temperature. However, analysis of the time-dependent populations of intermediates from the reference data (Schmidt *et al.*, 2013) confirms the equivalence of the two data sets, as data in both cases were collected at time delays in the plateau region at intermediate concentrations. On the microsecond timescale we observe the presence of a mixture of the pR_1/pR_{E46Q} and pR_2/pR_{CW} states. Although stronger electron-density difference signals were observed for the single-crystal data compared with our microfluidic results, we clearly observed the displacement of the S atom from Cys69 and the carbonyl group from the linked thioester group (Fig. 5a). On the millisecond timescale we observe changes in the electron density corresponding to the change in position of the phenolic ring in the pB_1 state (Fig. 5b). As expected, the electron-density difference maps comparing the dark and pB_1 state for these time-resolved data were less defined than for the experiment in which repeated pulse–probe cycles were used to accumulate high concentrations of pB_1 (Fig. 4).

In comparing the electron density obtained using traditional single-crystal methods with our serial microfluidic approach, we believe that the weaker electron density observed in our experiments is the result of parameters related to the signal-to-noise ratio of the X-ray diffraction data rather than a difference in reaction initiation efficiency. In traditional methods, which utilize large single crystals ($100 \times 100 \times 700$ µm), the optical density of PYP crystals is such that incident laser light is unable to effectively initiate the photocycle through the entire depth of the sample. In these experiments, the sample was aligned such that the X-rays only probed the laser-illuminated volume near the surface of the crystal, where photoinitiation is more efficient (60–80 µm). On-chip crystallization resulted in crystals with a typical thickness on the order of 10–60 µm, which is in the range where efficient photoinitiation can be achieved throughout the entire crystal volume. Furthermore, a higher incident laser power was used in our experiments (4.8 *versus* 4.0 mJ mm^{-2}) and our microfluidic chips are optically transparent and do not interfere with transmission of the laser signal. Thus, photoinitiation of the reaction should not be limiting in our experiments.

However, signal-to-noise considerations are particularly significant in the context of time-resolved experiments, where structural changes produce only small variations in the overall diffraction signal (Helliwell *et al.*, 1998; Ren *et al.*, 2013). Neglecting variations in crystal quality, signal to noise can be adversely affected by either attenuation of the diffraction signal itself or a mismatch in the size of the X-ray beam relative to the sample. Unfortunately, the overall size of our crystals ($10–60 \times 10–60 \times 100–300$ µm) was smaller than the X-ray beam size (90×70 µm), resulting in a higher background level. Matching the size of the X-ray beam to the crystal, either by growing larger crystals or by using a

microfocused X-ray beam, would improve the quality of the observed diffraction signal by eliminating this source of noise. Additionally, the materials used in our microfluidic device can attenuate the observed diffraction signal. Our current microfluidic chip design has a total material path length of 127 µm compared with a maximum crystal thickness of 60 µm (Perry *et al.*, 2014). This achieves a path-length ratio of device materials to crystal of approximately 2:1. Further optimization of the device architecture and manufacturing procedures would enable a significantly higher signal from the crystal and/or the analysis of microcrystals. Such efforts are ongoing.

4. Conclusions

The work reported here demonstrates the efficacy of a serial, microfluidic approach for time-resolved Laue crystallography. Laser initiation was an effective trigger of the PYP photocycle in the context of our optically transparent microfluidic devices. Small slices of diffraction data were merged to generate high-quality electron-density difference maps depicting the expected pR_1/pR_{E46Q} and pR_2/pR_{CW} states at 10 µs and the pB_1 state at 1 ms. This approach takes advantage of X-ray compatible microfluidic platforms to both grow a large number of high-quality, isomorphous crystals and to facilitate efficient, high-throughput serial time-resolved Laue diffraction analysis without the need for sample handling and mounting. This method has the potential to enable the study of structural dynamics for irreversible biochemical reactions. Short Laue exposures could also help to outrun secondary radiation damage (Warkentin *et al.*, 2013). Looking forward, the integrated fluid-handling capabilities of our microfluidic platform could be harnessed to enable chemical triggering (for example, substrate addition or a pH jump) to investigate a wide range of biologically and medically relevant protein targets that have thus far been resistant to time-resolved studies. Building on this idea, it would also be possible to extend these types of studies to multivariable analyses to expand the scope and context of the resultant dynamic structural information (Ren *et al.*, 2013).

References

Barends, T. R. M., Foucar, L., Botha, S., Doak, R. B., Shoeman, R. L., Nass, K., Koglin, J. E., Williams, G. J., Boutet, S., Messerschmidt, M. & Schlichting, I. (2013). *Nature (London)*, **505**, 244–247.

Borgstahl, G. E. O., Williams, D. R. & Getzoff, E. D. (1995). *Biochemistry*, **34**, 6278–6287.

Boutet, S. *et al.* (2012). *Science*, **337**, 362–364.

Brehm, W. & Diederichs, K. (2014). *Acta Cryst.* D**70**, 101–109.

Chapman, H. N. *et al.* (2011). *Nature (London)*, **469**, 73–77.

Cherezov, V., Rosenbaum, D. M., Hanson, M. A., Rasmussen, S. G., Thian, F. S., Kobilka, T. S., Choi, H.-J., Kuhn, P., Weis, W. I., Kobilka, B. K. & Stevens, R. C. (2007). *Science*, **318**, 1258–1265.

Cornaby, S., Szebenyi, D. M. E., Smilgies, D.-M., Schuller, D. J., Gillilan, R., Hao, Q. & Bilderback, D. H. (2010). *Acta Cryst.* D**66**, 2–11.

Dejoie, C., McCusker, L. B., Baerlocher, C., Kunz, M. & Tamura, N. (2013). *J. Appl. Cryst.* **46**, 1805–1816.

Demirci, H. *et al.* (2013). *Acta Cryst.* F**69**, 1066–1069.

Gati, C., Bourenkov, G., Klinge, M., Rehders, D., Stellato, F., Oberthür, D., Yefanov, O., Sommer, B. P., Mogk, S., Duszenko, M., Betzel, C., Schneider, T. R., Chapman, H. N. & Redecke, L. (2014). *IUCrJ*, **1**, 87–94.

Genick, U. K., Borgstahl, G. E. O., Ng, K., Ren, Z., Pradervand, C., Burke, P. M., Šrajer, V., Teng, T.-Y., Schildkamp, W., McRee, D. E., Moffat, K. & Getzoff, E. D. (1997). *Science*, **275**, 1471–1475.

Graber, T. *et al.* (2011). *J. Synchrotron Rad.* **18**, 658–670.

Guha, S., Perry, S. L., Pawate, A. S. & Kenis, P. J. A. (2012). *Sens. Actuators B Chem.* **174**, 1–9.

Hedman, B., Hodgson, K. O., Helliwell, J. R., Liddington, R. & Papiz, M. Z. (1985). *Proc. Natl Acad. Sci. USA*, **82**, 7604–7607.

Helliwell, J. R., Nieh, Y.-P., Raftery, J., Cassetta, A., Habash, J., Carr, P. D., Ursby, T., Wulff, M., Thompson, A. W., Niemann, A. C. & Hädener, M. A. (1998). *Faraday Trans.* **94**, 2615–2622.

Heymann, M., Opthalage, A., Wierman, J. L., Akella, S., Szebenyi, D. M. E., Gruner, S. M. & Fraden, S. (2014). *IUCrJ*, **1**, 349–360.

Hirata, K. *et al.* (2014). *Nature Methods*, **11**, 734–736.

Hunter, M. S. & Fromme, P. (2011). *Methods*, **55**, 387–404.

Hunter, M. S. *et al.* (2014). *Sci. Rep.* **4**, 6026.

Ihee, H., Rajagopal, S., Šrajer, V., Pahl, R., Anderson, S., Schmidt, M., Schotte, F., Anfinrud, P. A., Wulff, M. & Moffat, K. (2005). *Proc. Natl Acad. Sci. USA*, **102**, 7145–7150.

Johansson, L. C. *et al.* (2012). *Nature Methods*, **9**, 263–265.

Johansson, L. C. *et al.* (2013). *Nature Commun.* **4**, 2911.

Jung, Y. O., Lee, J. H., Kim, J., Schmidt, M., Moffat, K., Šrajer, V. & Ihee, H. (2013). *Nature Chem.* **5**, 212–220.

Kern, J. *et al.* (2013). *Science*, **340**, 491–495.

Kern, J. *et al.* (2014). *Nature Commun.* **5**, 4371.

Khvostichenko, D. S., Kondrashkina, E., Perry, S. L., Pawate, A. S., Brister, K. & Kenis, P. J. A. (2013). *Analyst*, **138**, 5384–5395.

Kort, R., Hoff, W. D., Van West, M., Kroon, A. R., Hoffer, S. M., Vlieg, K. H., Crielaand, W., Van Beeumen, J. J. & Hellingwerf, K. J. (1996). *EMBO J.* **15**, 3209–3218.

Kupitz, C. *et al.* (2014). *Nature (London)*, **513**, 261–265.

Liu, Q., Dahmane, T., Zhang, Z.-N., Assur, Z., Brasch, J., Shapiro, L., Mancia, F. & Hendrickson, W. A. (2012). *Science*, **336**, 1033–1037.

Liu, Q., Liu, Q. & Hendrickson, W. A. (2013). *Acta Cryst.* D**69**, 1314–1332.

Liu, Q., Zhang, Z. & Hendrickson, W. A. (2011). *Acta Cryst.* D**67**, 45–59.

Liu, W., Wacker, D. *et al.* (2013). *Science*, **342**, 1521–1524.

Liu, Z.-J., Chen, L., Wu, D., Ding, W., Zhang, H., Zhou, W., Fu, Z.-Q. & Wang, B.-C. (2011). *Acta Cryst.* A**67**, 544–549.

Lyubimov, A. Y., Murray, T. D., Koehl, A., Araci, I. E., Uervirojnangkoorn, M., Zeldin, O. B., Cohen, A. E., Soltis, S. M., Baxter, E. L., Brewster, A. S., Sauter, N. K., Brunger, A. T. & Berger, J. M. (2015). *Acta Cryst.* D**71**, 928–940.

McRee, D. E. (1993). *Practical Protein Crystallography*. San Diego: Academic Press.

Miller, R. J. D. (2014). *Science*, **343**, 1108–1116.

Moffat, K. (1997). *Methods Enzymol.* **277**, 433–447.

Moffat, K. (2014). *Philos. Trans. R. Soc. B Biol. Sci.* **369**, 20130568.

Neutze, R. & Moffat, K. (2012). *Curr. Opin. Struct. Biol.* **22**, 651–659.

Perry, S. L., Guha, S., Pawate, A. S., Bhaskarla, A., Agarwal, V., Nair, S. K. & Kenis, P. J. A. (2013). *Lab Chip*, **13**, 3183–3187.

Perry, S. L., Guha, S., Pawate, A. S., Henning, R., Kosheleva, I., Srajer, V., Kenis, P. J. A. & Ren, Z. (2014). *J. Appl. Cryst.* **47**, 1975–1982.

Redecke, L. *et al.* (2013). *Science*, **339**, 227–230.

Ren, Z., Bourgeois, D., Helliwell, J. R., Moffat, K., Šrajer, V. & Stoddard, B. L. (1999). *J. Synchrotron Rad.* **6**, 891–917.

Ren, Z., Chan, P. W. Y., Moffat, K., Pai, E. F., Royer, W. E., Šrajer, V. & Yang, X. (2013). *Acta Cryst.* D**69**, 946–959.

Ren, Z., Perman, B., Šrajer, V., Teng, T.-Y., Pradervand, C., Bourgeois, D., Schotte, F., Ursby, T., Kort, R., Wulff, M. & Moffat, K. (2001). *Biochemistry*, **40**, 13788–13801.

Ren, Z., Šrajer, V., Knapp, J. E. & Royer, W. E. (2012). *Proc. Natl Acad. Sci. USA*, **109**, 107–112.

Schmidt, M., Pahl, R., Srajer, V., Anderson, S., Ren, Z., Ihee, H., Rajagopal, S. & Moffat, K. (2004). *Proc. Natl Acad. Sci. USA*, **101**, 4799–4804.

Schmidt, M., Srajer, V., Henning, R., Ihee, H., Purwar, N., Tenboer, J. & Tripathi, S. (2013). *Acta Cryst.* D**69**, 2534–2542.

Schmidt, M., Šrajer, V., Purwar, N. & Tripathi, S. (2012). *J. Synchrotron Rad.* **19**, 264–273.

Schotte, F., Cho, H. S., Kaila, V. R. I., Kamikubo, H., Dashdorj, N., Henry, E. R., Graber, T. J., Henning, R., Wulff, M., Hummer, G., Kataoka, M. & Anfinrud, P. A. (2012). *Proc. Natl Acad. Sci. USA*, **109**, 19256–19261.

Smith, J. L., Fischetti, R. F. & Yamamoto, M. (2012). *Curr. Opin. Struct. Biol.* **22**, 602–612.

Stellato, F. *et al.* (2014). *IUCrJ*, **1**, 204–212.

Tenboer, J. *et al.* (2014). *Science*, **346**, 1242–1246.

Tripathi, S., Šrajer, V., Purwar, N., Henning, R. & Schmidt, M. (2012). *Biophys. J.* **102**, 325–332.

Wang, X. *et al.* (2012). *Nature Struct. Mol. Biol.* **19**, 424–429.

Warkentin, M., Hopkins, J. B., Badeau, R., Mulichak, A. M., Keefe, L. J. & Thorne, R. E. (2013). *J. Synchrotron Rad.* **20**, 7–13.

Yamaguchi, S., Kamikubo, H., Shimizu, N., Yamazaki, Y., Imamoto, Y. & Kataoka, M. (2007). *Photochem. Photobiol.* **83**, 336–338.

Yonath, A. *et al.*. (1998). *Acta Cryst.* A**54**, 945–955.

Zarrine-Afsar, A., Barends, T. R. M., Müller, C., Fuchs, M. R., Lomb, L., Schlichting, I. & Miller, R. J. D. (2012). *Acta Cryst.* D**68**, 321–323.